Hyper-Spectral Speckle Imaging of Resolved Targets

Fabien R. Baron, Stuart M. Jefferies, Dmitriy V. Shcherbik, Ryan Hall, Daniel Johns, and Douglas A. Hope
Georgia State University

ABSTRACT

We use numerical simulations to show that ultra-broadband speckle imaging (i.e., using a spectral bandwidth exceeding 500 nm) offers the potential for the simultaneous recovery of high-resolution spatial information and low-resolution spectral information[1] for resolved targets, using ground-based telescopes. This result opens the door for improved identification and characterization of targets, from LEO to GEO, and studies of the aging of materials in space.

1. BACKGROUND

Ground-based imaging plays a crucial role in Space Domain Awareness by providing essential information about objects in the near-Earth space environment. It serves two primary purposes: detecting faint objects and characterizing and identifying brighter objects. Accurately characterizing and identifying an object depends on achieving a high signal-to-noise ratio (SNR) in the observations and requires observations over a wide spectral range. This requirement is because precise characterization and identification need detailed spatial *and* spectral information. However, since the objects of interest often move rapidly, we must acquire spectral and spatial information within a short time frame. That is, we need *snapshot* hyper-spectral imaging capability.

To address this challenge, we aim to significantly increase the spectral bandwidth of speckle imaging observations of space-based targets at visible and near IR wavelengths over those typically made using standard filters[2]. We will then take advantage of the fact that dispersion in the Earth's atmosphere, perturbations in the wavefront introduced by the atmosphere, and diffraction in our imaging instrument all spread the light out differently at different wavelengths: i.e., they collectively act as a sort of spectrometer. We aim to use this approach to perform hyper-spectral speckle imaging of resolved targets in the near-Earth space environment. We note that the Air Force currently does not have multi-wavelength imaging capability as a part of routine operations, and a robust broadband speckle imaging system would only require minor modifications to existing Air Force imaging systems.

2. NUMERICAL SIMULATIONS

For our initial studies, we simulate observations of a satellite acquired with a 3.6m telescope[3] through atmospheric turbulence demonstrating Kolmogorov statistics. The field of view is sufficiently small that we can use the isoplanatic imaging model.

Our generic model satellite, which we only loosely base on an actual satellite, comprises three materials: anti-reflection coated solar panel, Kapton, and Aluminized Mylar (see Fig. 1). The spectra for these materials are those reported in [1]. Some of the Mylar and Kapton pixels have spectra representing the materials after they have been aged by "space weather."

To simulate broadband observations, we generate speckle image data for several wavelengths in the spectral range from 400 nm to 984 nm and then integrate these data over wavelength to form a broadband speckle image. This wavelength

[1] $\bar{\lambda}/\Delta\lambda \sim 12-78$ where $\bar{\lambda}$ is the mean observing wavelength and $\Delta\lambda$ is the spectral bandwidth of a measurement.

[2] Observations of the reflected sunlight from an object with a Lambertian reflection surface, using a camera with a QE curve that peaks at 0.6 at 580 nm, without any filter, provides $\sim$ x4 more photons than observations taken through a V-band filter with a FWHM of 90 nm. This increase in the photon count will improve the SNR for target detection. The increased spectral range of the observations facilitates the characterization of targets through their spectra.

[3] Similar size aperture to the Air Force's assets at SOR and AMOS

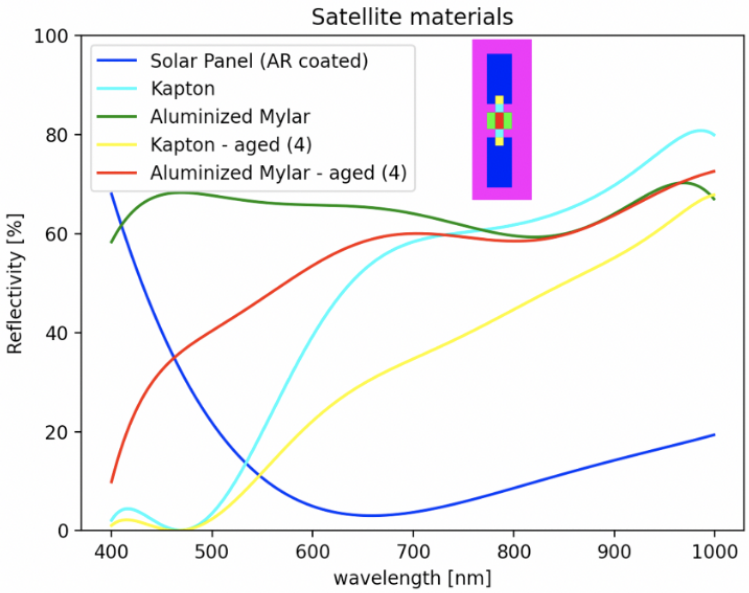

Fig. 1: Spectra for three different materials and for different aging of two of the materials. The inset shows location of each type of material in the toy satellite model.

bandpass corresponds roughly to the sensitivity range for silicon-based detectors. Depending on the simulation (with or without shot noise, see further in the text), we use 39 or 78 wavelengths. We incorporate dispersion effects using the model described in [3] and [4]. We then generate a time series of broadband speckle images, assuming that each image represents an independent realization of atmospheric turbulence.

To determine the potential performance of our technique, we simulate observations acquired in different turbulence conditions, measured by the atmospheric coherence length/Fried parameter r_0 over the range 10 cm $\leq r_0 \leq$ 25 cm at 500 nm and zenith angles, η, over the range $0 \leq \eta \leq 45$ degrees. We note that the median value of r_0 for nighttime observations from Mount Haleakala on Maui is 17 cm at 500 nm during the winter [2]. Fig. 2 shows some example broadband images.

Fig. 2: Five example (simulated) broadband data frames (400 nm $\leq \lambda \leq$ 984 nm.) for observations with a 3.6m aperture at an zenith angle of 0 degrees through turbulence with r_o = 17 cm at 500 nm. We use a negative color table to better highlight the speckle structure.

3. ANALYSIS APPROACH

In general, we do not have information on the details of the atmospheric blur, and we need to use the well-known approach of blind deconvolution [6, 9] for the recovery of the object and point-spread function (PSF) intensity distributions at each wavelength for every image. Inspection of the problem to be solved shows that we are dealing with a

situation with $N_{im}N^2$ measurements and $\left(N_\lambda N^2 + N_{im}N_\lambda N^2\right)$ variables. For the latter, the first term is associated with modeling the object, assuming it is stationary during the period of observation, while the second is associated with modeling the PSFs. Here N_{im} is the number of broadband images in the time series, N is the number of pixels along the side of the square 2D arrays used to model the intensity distributions of the object and PSFs, and N_λ is the number of spectral bands to be recovered.

It is clear that the ratio of the number of variables to the number of measurements

$$R = \frac{N_\lambda}{N_{im}} + N_\lambda \tag{1}$$

is highly unfavorable since we ideally would like $R \leq 1$. The situation is dramatically improved if we have some knowledge of the PSFs. Here, the additive N_λ term is removed from the ratio, and $R \leq 1$ is satisfied for $N_{im} \geq N_\lambda$.

We start with this situation to see if we can unscramble a set of broadband speckle images to reveal the wavelength dependence of the object when we have information on the PSFs, i.e. we start with the forward deconvolution problem. Here, we look at two different scenarios. The first, which is impractical but allows us to examine the feasibility of our proposed technique under idealized conditions, is where we assume we have perfect knowledge of the wavefronts and do not have photon ("shot") noise or camera read noise: we just have atmospheric turbulence "noise." In this scenario we reconstruct a 512×512 pixel object at each of the 78 wavelengths used to generate the 100 frames broadband focal plane images that constitute the data. The second scenario is where we have access to simultaneous wavefront sensor data, and there is photon and read noise on the broadband image data. The availability of wavefront sensor data allows us to perform *deconvolution from wavefront sensing* [7]. However the presence of shot noise increases the number of frames needed to recover a $512 \times 512 \times 78$ pixel source well beyond a few hundred frames, significantly increasing the computational cost. For this proof-of-concept work we consequently set the simulation to reconstruct a $256 \times 256 \times 39$ pixel object instead.

4. RESULTS

Examples of data frames generated are shown in Fig. 2. The results for the first scenario, from a forward deconvolution of five sets of 100 frames of data assuming perfect knowledge of the wavefronts, are shown in the middle row of Fig. 3 and Fig. 5. From a morphology standpoint, the reconstructed images of the object at the different wavelengths are superior to those for observations we could obtain without atmospheric turbulence, i.e., observations demonstrating spatial resolutions commensurate with the diffraction limits at each wavelength. This improvement is due to the spatial frequency information in the recovered images, inside the diffraction-limited cutoff at each wavelength, having amplitudes that are restored to a level that is above that in the diffraction-limited observations (see Fig. 4). There is also some level of detectable super-resolution.

Figure 5 highlights the fidelity of the spectral recovery in the non-zero intensity pixels in the true object, and suggests that broadband speckle imaging has strong potential as a tool for ground-based hyper-spectral imaging of targets in space. Moreover, as we find clear differences in the spectral signals for materials with and without weathering effects, which are evident in our reconstructions but not so much so in the traditional diffraction-limited resolution images (e.g., the red and green curves). Broadband imaging may consequently offer a way forward for studying the aging of materials of targets on orbit. We note that the results shown in Figs. 3, 4, and 5 are not sensitive to the values of r_0 and η studied.

The next step in this work is to ascertain the spatial and spectral fidelity of our reconstructions in the second scenario of *noisy* observations of spatially extended objects, and with limited knowledge of the PSFs. Our experience with the blind deconvolution of noisy monochromatic data tells us that we should investigate the restoration of aperture diverse speckle data [5]. This is because the blind deconvolution algorithm is susceptible to entrapment in local minima when dealing with noisy data. A simple implementation of aperture diversity is to split the incoming photons into two channels, a full aperture channel and a channel where a micro-lens array samples the aperture. The latter acts as a focal plane wavefront sensor[8]. Here, we use wavefronts in our reconstruction that have r.m.s.e. values commensurate with those expected from an imaging Shack-Hartmann wavefront sensor viewing through $D/r_0 \sim 20$ conditions, i.e., σ_{rmse} =0.2 radians [8]. The target is assumed to have a brightness of mag +4, and the CCD camera has 2e- of read noise.

The results in Fig. 6 show a degradation with respect to those shown in Fig. 5, as expected. The difference between

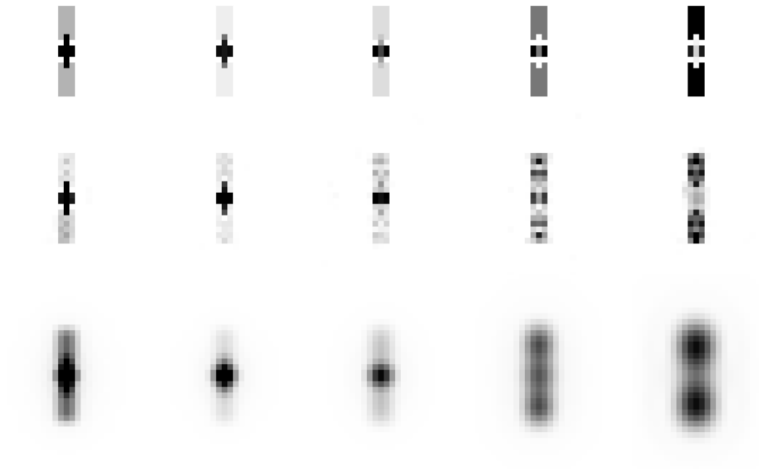

Fig. 3: Top row: The true intensity distributions at (left to right) 400 nm, 474 nm, 582 nm, 753 nm, and 984 nm. Middle row: The corresponding recovered intensity distributions from 80 data frames and 1,000 iterations. The zenith angle was 0 degrees, the telescope aperture was 360 cm, and r_0 = 17 cm. Bottom row: The corresponding intensity distributions for observations with diffraction-limited resolution.

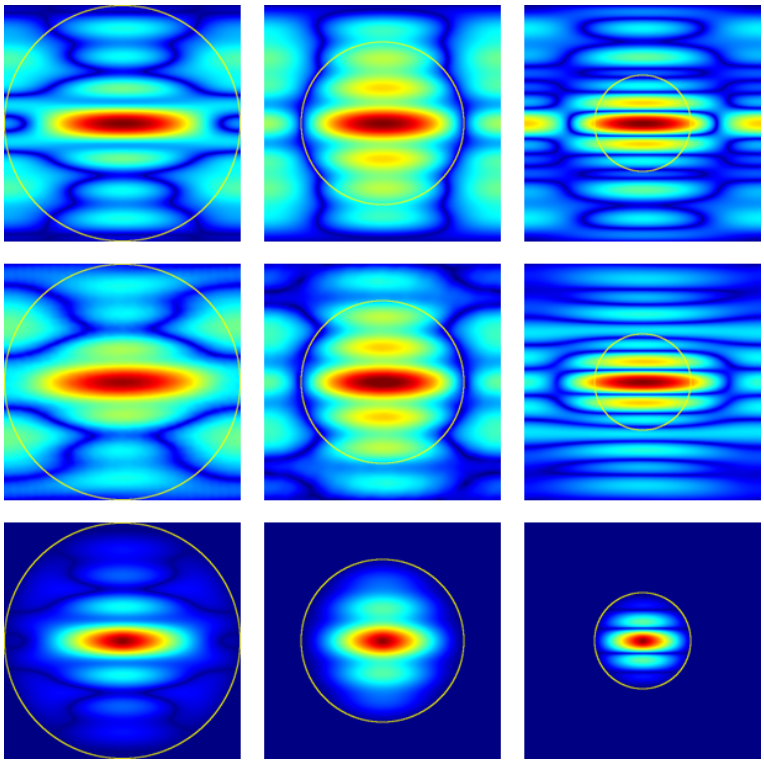

Fig. 4: The true, recovered, and diffraction-limited (top-to-bottom) Fourier amplitude spectra of the object at 400 nm, 582 nm, and 984 nm (left to right). The yellow circles denote the diffraction-limited cutoff frequency. Amplitudes are displayed on a square root scale.

the two will be reduced as soon as we allow the wavefronts to be updated during restoration, that is when we move to a blind deconvolution algorithm. However, as shown by Eqn. 1, this involves a significant increase in the number

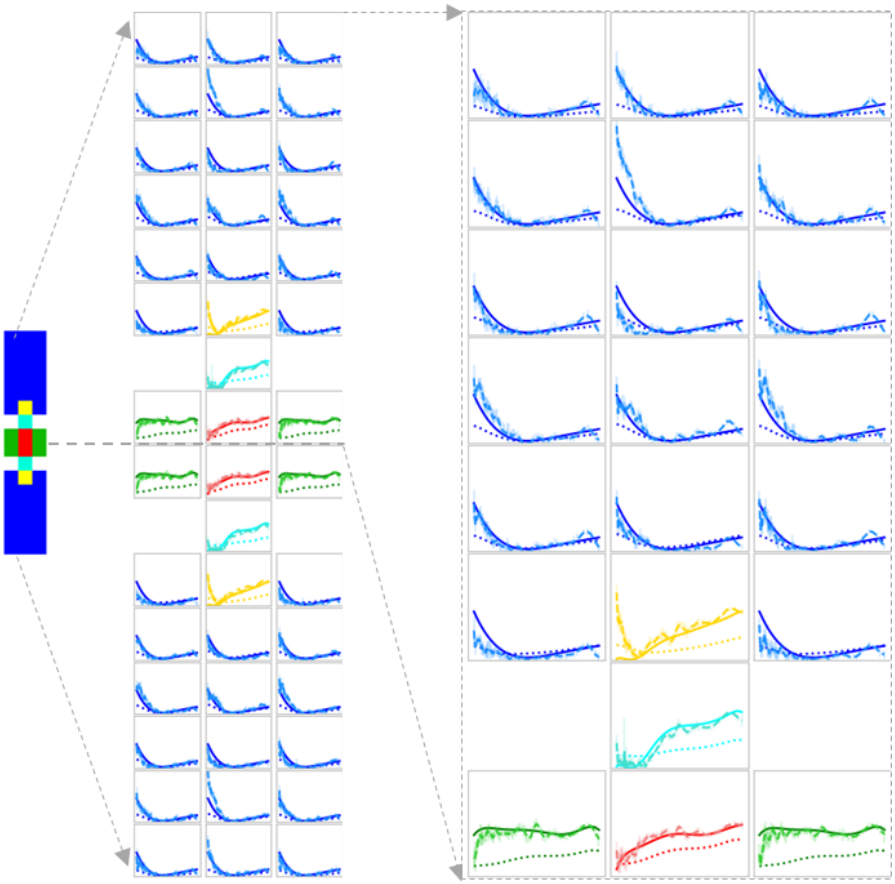

Fig. 5: This figure shows the true and recovered spectra at the different spatial locations in the target object. For the spectral plots the x-axis denotes wavelength, going from blue to red (left to right) in 78 wavelength steps and the y-axis is intensity (increasing vertically). The true spectra are shown with solid lines using the color scheme adopted in Fig. 1 for the different materials, the recovered spectra are shown by the dashed lines with 1 σ error bars, and the observations with diffraction-limited resolution are shown by the dotted lines. The zenith angle for the observations is 0 degrees, the telescope aperture is 360 cm, and r_0 = 17 cm. The wavefronts are assumed to be known. The right-hand side of the figure shows a blow up of the top half of the satellite. The recovered spectra in the bottom half are identical to those in the top half.

of variables. An intermediate step could be to use the approximation that the phase perturbations at each wavelength, $\phi(\mathbf{u})$, for a given realization of the atmosphere, can be modeled using a single optical path difference (OPD ($\mathbf{u}$), i.e.,

$$\phi(\mathbf{u}) = 2\pi \frac{OPD(\mathbf{u})}{\lambda} \; . \tag{2}$$

In this case, $R = \frac{N_\lambda}{N_{im}} + 1$. Once a solution is found, we can then move to modeling the individual phase perturbations at each wavelength. What is clear is that efficient implementation of the blind algorithm will require some research. Even so, the deconvolution from wavefront sensing results still show that we can potentially recover useful pixel-by-pixel spectral information on the target.

We note that in this second scenario, we introduced an unresolved target a small distance away from the satellite with a brightness of mag +9. Not only could we detect the presence of this unresolved "closely spaced object" (CSO) source in our reconstruction, but its recovered spectral behavior showed indications of its solar panel composition (see Fig. 7). Our broadband observations contain 3.7 times more photons than would be obtained using a traditional V-band filter with an FWHM of $\sim$ 90 nm (assuming reflected solar light and solar panel material). This increase in the photon count helps significantly with the detection of faint objects: 97% of the source's total flux is recovered in the pixel

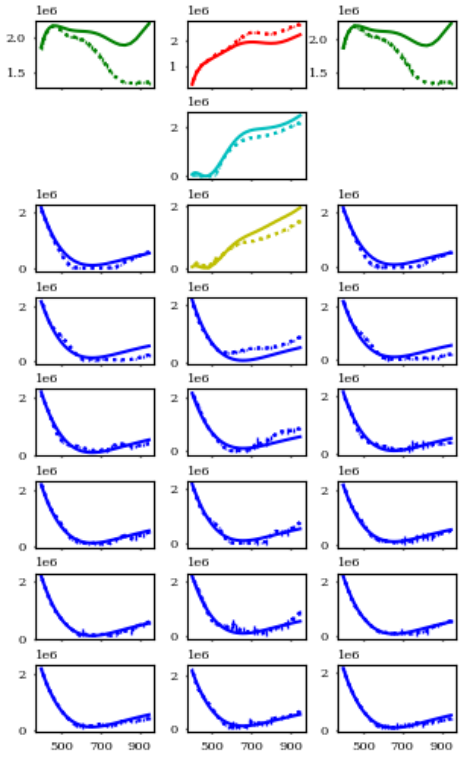

Fig. 6: This figure shows the spectra in each pixel of the reconstructed target for the second scenario, i.e. for data including shot noise reconstructed using wavefronts estimated from independent imaging Shack-Hartmann wavefront sensor measurements. The x-axes are wavelengths, going from blue to red (left to right) in 39 wavelength steps. The y-axes are intensity (increasing vertically). The true spectra are shown with solid lines using the color scheme adopted in Fig. 1 for the different materials and the recovered spectra are shown by the dashed lines with 1 σ error bars. The zenith angle for the observations is 17 degrees, the telescope aperture is 360 cm, and r_0 = 17 cm. The satellite has a brightness of mag +4.

where the CSO is located, and more than 99.5% within the 3×3 pixel zone around. We estimate that the absence of nearby materials prevents spectral mixing and thus eases the reconstruction.

5. DISCUSSION AND FUTURE DIRECTIONS

We have used numerical simulations to show that ultra-broadband speckle imaging offers the potential for the simultaneous recovery of high-resolution spatial information and low-resolution spectral information for resolved targets using ground-based telescopes. This result opens the door for improved identification and characterization of space-based targets and studies of the aging of materials in space.

Once we have fully determined the performance of blind deconvolution of aperture-diverse, narrow field-of-view, ultra-broadband (noisy) speckle data, we will extend our investigation to targets that require a field-of-view that can no longer be considered isoplanatic. [8] have shown that aperture-diverse measurements can provide a tomographic measure of the wavefront phase and amplitude that can be used to restore anisoplanatic imagery.

We also note that spectral mixing is inevitable. This is demonstrated in Figs. 3 and 5, where observations with diffraction-limited spatial resolution highlight that the intensity observed in a pixel represents the combination of the signals from multiple surrounding pixels, where the number of surrounding pixels that contribute increases with increasing wavelength.In addition, spectral mixing will still occur when there are changes in material over distances smaller than the pixel size. Despite the inevitability of spectral mixing, we want to minimize it as far as possible. Ideally, we want to achieve a level of super-resolution such that any diffraction-related effects remaining in the re-

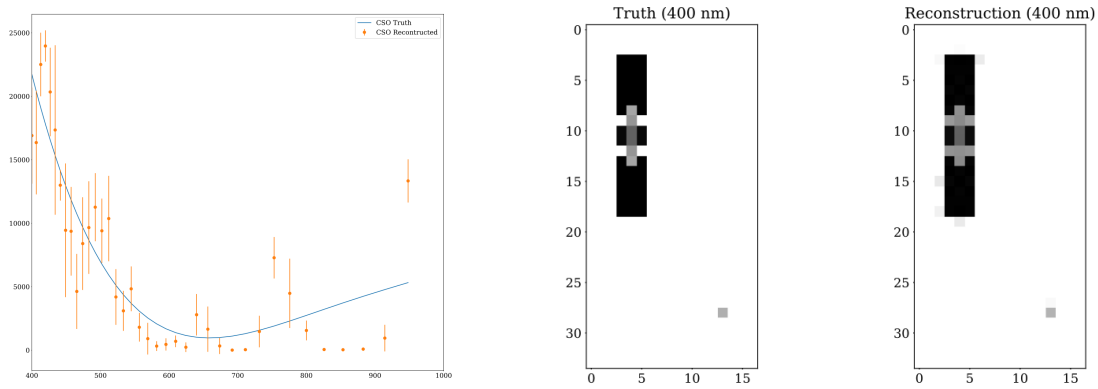

Fig. 7: Left: this figure shows the spectra in each pixel of the unresolved CSO (mag +9 source). Right: reconstruction of the CSO alongside the satellite, shown to the power of 0.25 to enhance contrast. The CSO flux is at the level of the artifacts in the main source but its separation from the satellite allows for an accurate reconstruction.

constructed data negligibly contribute to the mixing. On this subject [10] has shown that aperture modulation (i.e., aperture diversity) can provide a significant level of super-resolution for high SNR observations when the point spread function is accurately known and static. Although the latter is not the case we have with speckle imaging, if we can accurately recover the amplitudes of the spatial frequencies inside the cutoff frequency for both the target object and the PSFs, we may be able to use the technique of [10] to provide some usable level of super-resolution. We plan to investigate this possibility.

Lastly, since the only imposed prior during the reconstruction is positivity, regularization of the solutions should greatly improve the spectral fidelity. To this end we are investigating the use of the alternating direction method of multipliers (ADMM) to tackle several aspects of the deblurring process, including the parallelization and distribution of the computation (currently difficult with our gradient approach) and the spectral unmixing problem.

6. ACKNOWLEDGEMENTS

This material is based upon work supported by the Air Force Office of Scientific Research under award number FA9550-21-1038. Any opinions, findings, conclusions, or recommendations expressed in this material are those of the authors and do not necessarily reflect the views of the United States Air Force.

7. REFERENCES

[1] Miles Bengtson, Jordan Maxwell, Ryan Hoffmann, Russell Cooper, Stephanie Schieffer, Dale Ferguson, W. Robert Johnston, Heather Cowardin, Elena Plis, and Daniel Engelhart. Optical Characterization of Commonly Used Thermal Control Paints in a Simulated GEO Environment. In S. Ryan, editor, *The Advanced Maui Optical and Space Surveillance Technologies Conference*, page 33, September 2018.

[2] L. W. Bradford. Maui4: a 24 hour Haleakala turbulence profile. In *The Advanced Maui Optical and Space Surveillance Technologies Conference*, 2010.

[3] C. D. Coleman, W. R. Bozman, and W. F. Meggers. Table of wavelnumbers: 7000 a to 1000 μ. Technical report, U.S. Department of Commerce, National Bureau of Standards, 1960.

[4] A. V. Filippenko. The importance of atmospheric differential refraction in spectrophotometry. *Publications of the Astronomical Society of the Pacific*, 94:715–721, August 1982.

[5] Douglas A. Hope, Stuart M. Jefferies, Michael Hart, and James G. Nagy. High-resolution speckle imaging through strong atmospheric turbulence. *Optics Express*, 24(11):12116, May 2016.

[6] Stuart M. Jefferies and Julian C. Christou. Restoration of Astronomical Images by Iterative Blind Deconvolution. *The Astrophysical Journal*, 415:862, October 1993.

[7] Stuart M. Jefferies, Michael Lloyd-Hart, E. Keith Hege, and James Georges. Sensing wave-front amplitude and phase with phase diversity. *Appl. Opt.*, 41(11):2095–2102, Apr 2002.

[8] Daniel Johns, Douglas A. Hope, Fabien R. Baron, Stuart M. Jefferies, and Dmitriy Shcherbik. Performance of an Imaging Shack-Hartmann Wavefront Sensor. In *The Advanced Maui Optical and Space Surveillance Technologies Conference*, September 2023.

[9] Timothy J. Schulz. Multiframe blind deconvolution of astronomical images. *J. Opt. Soc. Am. A*, 10(5):1064–1073, May 1993.

[10] Biao Xu, Zhiqiang Wang, and Jinping He. Beating the Rayleigh limit via aperture modulation. *Journal of Optics*, 23(1):015701, January 2021.